Lagrangian Pathways and Connectivity in a Reef Canopy

Effects of organism spacing and waves

Reint Fischer

A thesis presented for the degree of
Master's in Physics

IMAU
Utrecht University
Netherlands
July 2020

Abstract

Changing global ocean conditions threaten many tropical reef ecosystems. Affected reefs in turn change the local ocean conditions. Local changes in bottom friction, nutrient availability, oxygen consumption and spreading of spawn and diseases determine the transient response of these ecosystems to changing global conditions. To study the mechanisms causing a decrease in coral cover in many reefs including those in the Caribbean, more detailed models of the complex turbulent flow over the reef seafloor are starting to be developed. This study aims to develop Lagrangian tools to analyze the small-scale transport processes and the network of sedentary organisms, the immobile organisms that depend entirely on the flow. This enables studying the local mechanisms driving past and future reef ecosystem changes. Virtual particles are released and tracked in model output of the unsteady flow over a reef canopy. Using a novel scheme for the particle boundary conditions, continuous pathways are traced near the organism surfaces to study the influx and exchange of particles and solutes to and from the sedentary organisms. The decrease of coral organisms is shown to increase entrainment of water from higher up in the water column by eddies that become larger as the spacing between large coral organisms increases. This also promotes the exchange of particles and solutes between smaller organisms in the wake of larger organisms. Waves interact with the larger spacing between organisms and further increase the eddy size and strength. Waves also increase the length scale of influence for individual organisms.

Acknowledgements

As valuable as this thesis is to my master's degree and to my first contributions as a young scientist, much more so do I personally value the experience of working in an academic environment. For both their contributions to the work behind this thesis and to the pleasure it was to learn from them, I want to thank the people who have supported me. Specifically, Dr Erik van Sebille, my supervisor, for creating a wonderful working environment, for helping me develop as a scientist and as a person and for being understanding. Dr Paolo Stocchi and Dr Adam Candy made this thesis possible by providing me with the data generated specifically for this thesis. Their work inspires me to discover the possibilities in oceanography driven by scientific creativity and curiosity. They have spent invaluable hours discussing my work with me and I thank them for their hospitality at NIOZ.

The experience of working in an environment where science is a joint endeavour has been the most enjoyable part of my thesis. I want to thank the members of the *OceanParcels* group for allowing me to walk into their offices to talk to them about my work, for sharing their research, code and enthusiasm. Especially Daan Reijnders has repeatedly thought along with me and discussed the science and the algorithms, while Christian Kehl has been very supportive with my coding problems and fed my enthusiasm for visualization practices.

Lastly I want to thank my girlfriend Evelien Castrop, for being incredibly strong and supportive in an eventful year. She, as well as my parents and siblings, has given me all the space I needed to work from home during the Covid-19 pandemic.

Contents

Chapter 1

Introduction

Anthropogenic activities have affected coral reefs in many foreseen and unforeseen ways. Pushing the extreme heat tolerance of species (Leggat et al., 2019), ocean acidification (Anthony et al., 2008; Hoegh-Guldberg et al., 2007) and the increased prevalence of oxygen-poor regions (Altieri and Gedan, 2015; Blakeway, 2018) are examples of threatening global developments. Locally, overfishing and pollution can create even larger disturbances of the environment (Hughes et al., 2003; Hughes, 1994).

As a reef ecosystem responds it in turn influences the local ocean conditions. It can regulate the local chemical composition of for example oxygen and particulate and dissolved organic matter (Haas et al., 2010), but also of pH and aragonite saturation (Andersson et al., 2014). The local hydrodynamics depend on the geometry of the reef (Yu et al., 2018; Özgökmen et al., 2004). The response can be seen as a feedback between changing local ocean conditions and changing local reef conditions that influence each other (figure 1.1).

The anthropogenic forcings imposed on specific local conditions can have many different long-term consequences for the local environment depending on the reef ecosystem feedback response. Because ecosystems can be very complex and varying from region to region, understanding their response and long-term development is extremely challenging. Results of long-term observations document the response and the widespread loss of coral cover in reef ecosystems. Their place in reefs is taken by other groups such as macroalgae and cyanobacterial mats (de Bakker et al., 2017). These results inspire the development of hypotheses and theories on the specific mechanisms that enable these shifts in species distributions (Silveira

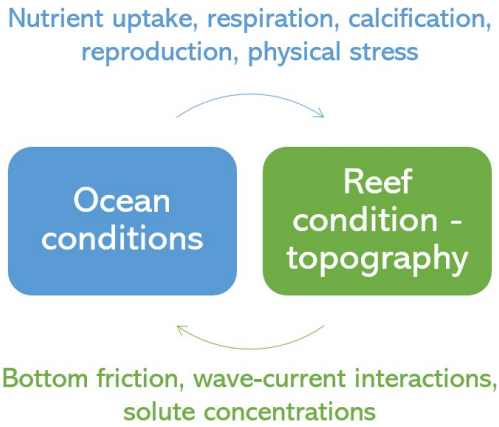

Figure 1.1: Ocean conditions and reef ecosystem changes interact in a feedback loop. Global anthropogenic forcing incites local response feedback in reef ecosystems.

et al., 2018).

The research on the mechanisms in which hydrodynamic conditions affect reef species focus mainly on the nutrient uptake at different flow velocities (Osinga et al., 2017; Pujol et al., 2019) and chemical composition (Silveira et al., 2018; Haas et al., 2010). The effects of a reef on the hydrodynamics are largely in dissipating energy by bottom friction. This can protect coasts from erosion and influences the behaviour of surface waves, tidal waves and coastal currents. The material and geometrical properties of the reef affect canopy flow velocities (van Rooijen et al., 2020; Asher and Shavit, 2019; Lowe et al., 2005b) and bottom friction (Duvall et al., 2020; Özgökmen et al., 2004).

From the point of view of the reef and the sedentary organisms that make up the reef, the hydrodynamics are mainly important as the transport mechanism for nutrients, oxygen, larvae, diseases and other biochemically active particles. Sedentary organisms are organisms that are fixed in one place and therefore depend entirely on the flow and the local seafloor for their well-being. At the same time, their immobility makes them 'permanent' features in the velocity field. Examples of sedentary organisms in reef ecosystems are scleratinian corals, crustose coralline algae, sponges, macroalgae and cyanobacterial mats. The research presented here aims to study the pathways of transport towards these sedentary organisms. Together they form the reef canopy.

To study the advection-based processes like feeding, respiration, reproduction and spreading of microbes and diseases in reef canopies, we can use Lagrangian analysis of the velocity field to discover changes in the local influx of these important particles and chemical compounds. The Lagrangian approach integrates particle velocities to trace the pathways of particles or water masses in a time-dependent flow. Lagrangian tools are frequently used at an ocean scale to map plastic waste distributions (van Sebille et al., 2020; Maximenko et al., 2019), to track oil spills (Mariano et al., 2011; Azevedo et al., 2009), coherent water masses (Suara et al., 2020; Haller, 2015) and other transport problems. Here, the transport that sedentary organisms depend on will be visualized and quantified.

Apart from studying the flux of particles to the different sedentary organisms, Lagrangian analysis can be applied in another way that nicely complements existing research on an ecosystem level. Ecosystems are often analysed as complex networks of actors and links between them. The actors can be predators and prey or individuals in a population linked by reproduction. Lagrangian pathways can be interpreted as the physical connection linking the sedentary organisms in a network. This network then describes how changes in an individual organism affect the organisms around them: at what time scales and length scales. Network theory is already being applied to Lagrangian trajectories on larger scales to analyse larval dispersion (Edwards et al., 2006; Vic et al., 2018) or to define coherent ocean regions as marine protected areas (Della Penna et al., 2017; Delpeche–Ellmann and Soomere, 2013).

Studying the seafloor hydrodynamics at the scale of individual organisms is becoming feasible due to increasing computer power and large improvements in photogrammetry: using photos to create a 3D model (Parra Peñuela et al., 2019; Aati and Nejim, 2020; Chen et al., 2019). The 3D models of parts of a reef that have

been monitored for decades can give very detailed insights in the hydrodynamics at a specific location.

To discover the possibilities of using Lagrangian techniques to investigate the transport processes at the scale of individual sedentary organisms, this study aims to find the challenges of tracing particle trajectories at this scale, to develop the concepts that illuminate the mechanisms important for the transport processes and to test these concepts on two environmental parameters relevant in literature. Coral cover has decreased significantly in many reefs globally and specifically in the Caribbean (Jackson et al., 2014; de Bakker et al., 2017; Rogers and Miller, 2006; Sweatman et al., 2011). To understand how this decrease in coral cover may affect the transport processes, the concepts developed in this study are compared for a flow over a densely populated simplified reef canopy and a similar seabed with some of the coral-like objects taken out. The second environmental condition investigated to test the Lagrangian concepts is the influence of waves. Since a large part of the literature on hydrodynamics over reefs concerns the dissipation of wave-energy (Lowe et al., 2005a; Monismith et al., 2015; Péquignet et al., 2011; Harris et al., 2018), it is valuable to test the effect of waves on the Lagrangian concepts.

This leads to the following research questions:

- What are challenges to using Lagrangian techniques in an environment the scale of individual reef organisms?
- How can Lagrangian volume fluxes illuminate the mechanism by which respiration of sedentary organisms is influenced by the hydrodynamics?
- How are sedentary organisms locally connected by the flow? What are length scales and time scales at which changes in one organism affect their local neighbourhood?
- What are the effects of waves and decrease in coral cover on the metrics developed to study transport processes and local connectivity?

In the methods section the modelling setup will be elaborated upon and all processing steps will be explained. As the main focus of the research questions is on the development of the Lagrangian metrics to study advection and connectivity, the results and discussion will be structured based on these metrics and not based on the conclusions regarding the effects of waves and coral cover. For a concise summary of the effects of either waves or coral cover I refer to the conclusion.

Chapter 2

Methods

To quantify the Lagrangian pathways and define the network of sedentary organisms a number of process steps are necessary. The flow data on which the particle trajectories are based come from a numerical simulation of a Computational Fluid Dynamics (CFD) model run at NIOZ (Royal Netherlands Institute for Sea Research). The output of this model needs to be processed to distinguish the coral-like objects in the flow and to determine the distance and direction to these objects within the fluid domain, based on which the particle movement will be parameterized and analysed. Particle tracking simulations are the basis for the volume fluxes and the network definition. The trajectories need to be processed once more after the simulation to generate the network. These procedures are best described in four parts: running the CFD model, the preprocessing steps, the particle tracking simulation and the postprocessing steps. Apart from the CFD modelling, which was not done by me, all the code for the implemented methods and analysis is available at github.com/OceanParcels/CoralDispersion

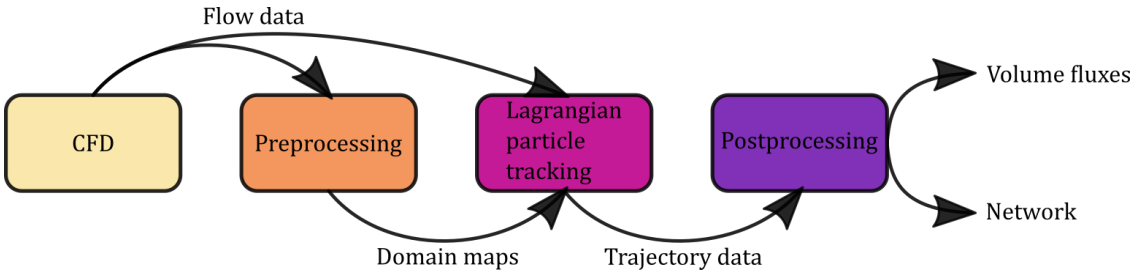

Figure 2.1: Workflow of the thesis. The coloured boxes show the different steps and the arrows show the data products as input and output of the different steps

2.1 CFD model

The software used to run the CFD model by researchers at NIOZ is *Gerris*. It is a free and open-source software that solves the incompressible 2D or 3D Navier-Stokes equations by parameterising turbulence in a bulk viscosity. The 2D model domain

is based on the cross-section of a flume experiment in the xz-plane. The domain is 1 m in the z-direction and 9 m in the x-direction. The resolution of the grid is 0.015625 m in either direction. This is not small enough to solve the turbulent energy dissipation to the Kolmogorov scale, which limits the realism of the model compared to seawater. The output is generated at timesteps of 1 second. This is very coarse given the spatial resolution and the velocities that go up to 1 m/s, because changes in the flow that occur at $\mathcal{O}(1\,\mathrm{m\,s^{-1}})$ travel through multiple steps of Δx in one timestep. This means that for explicit time integration schemes, the model setup does not satisfy the Courant-Friedrich-Lewy condition (see equation 2.3 in section 2.3.1).

The free stream velocity prescribed at the upper boundary is 1 m/s, near the maximum of realistic values for deeper Caribbean reefs (Candy, 2020; Gyory et al., 2013). Surface waves are modelled by attenuating the horizontal velocity at the upper boundary with periodic motion with a frequency of 6 s. The vertical velocity profile prescribed at the upstream boundary is parabolic from 1 m/s at the top to 0 m/s at the bottom.

To model the flow over a reef canopy at the scale of photogrammetric models being developed, coral-like objects were placed in the domain of the flume experiment (figure 2.2). The placement of these objects has two important features: the height of the tallest objects increases downstream, effectively creating a slope up which the current flows. The second feature is the effective object spacing. The domain can essentially be divided in two parts: in the first objects have similar sizes and shapes, while in the second large and small objects alternate. The small objects effectively create a spacing between the larger objects into which water could flow more easily than between the objects in the first part of the domain.

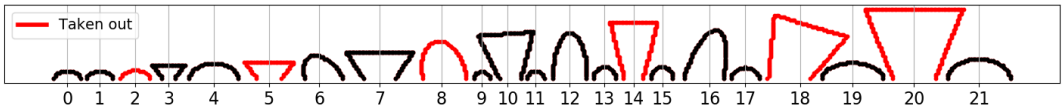

Figure 2.2: The placement and numbering of coral-like objects in the domain. One simulation contains all 21 objects. The other has the red objects removed to model the decrease of coral cover.

To model the decrease of coral cover one object was taken out in every $\pm$ 1 m in the domain. The objects that were taken out are drawn in red in figure 2.2.

2.2 Preprocessing

Corals and other sedentary reef organisms interact with the particles and biochemical solutes advected by the flow in a number of different ways. Many corals have tentacles that can catch plankton, biologically active particles may stick to surfaces, while solutes diffuse in the so-called diffusive boundary layer surrounding organism surfaces. Because these processes are not modelled in this study, interaction with objects is based on the distance to the model surface. The different interactions

occur at different distances from the organism. Diffusive boundary layers are in the order of millimeters while tentacles can be centimeters long. Since the length of the gridcells is ± 1.5 cm, the motions beneath this scale are not resolved. The interaction distances studied here are therefore varied between 5 and 2 cm. This implies that the results presented in this thesis are valid for a broad definition of particles that possibly interact and might include many particles that would not interact in specific processes.

Four tasks are performed in preprocessing. First (2.2.1), the objects need to be defined to be able to analyse each object separately. Then, the fluid domain is mapped with the distance towards the nearest object (2.2.1) and a voronoi diagram (2.2.3), showing which object is nearest. These are tasks two and three. This way, the nearest object to each particle is known, including the distance to it. From this we can analyse the particles based on their presence in an interaction layer of one of the objects. By sampling the maps during the particle tracking simulation instead of calculating these distances during the simulation, the trajectories can easily be filtered by their relationship to the different objects and the computing time is kept to a minimum. Finally, the fluid cells are mapped according to the orientation of the bordering cells that represent the solid objects (2.2.4). The orientation of the local solid-fluid boundary determines how the local boundary conditions for the particles are satisfied (section 2.3.1).

2.2.1 Defining the numbered set of objects

The first step in the preprocessing of the flow data is separating the objects. The flow data consists only of the velocity field in time and space. The velocities at the solid cells that represent the objects are represented by NaNs. From these invalid numbers we want to find the coordinates drawing the different objects. For the full description of the algorithm, visit github.com/OceanParcels/CoralDispersion.

To draw the objects, only the coordinates cells that define the surface of the object need to be known. Once the invalid cells are mapped to the grid, the inner cells that are surrounded by the other invalid cells or the edge of the grid are removed from the map to leave only the object surfaces. Then the algorithm loops through the domain looking for invalid cells, and once one is found, it checks the neighbouring cells for the connections drawing the surface. The surface can extend in two directions. Once no neighbouring invalid cells can be found, the coordinates of the entire surface found are stored and those cells are removed from the domain that is still to be scanned for other objects. This results in the stored coordinates for 21 objects shown in figure 2.2.

2.2.2 Mapping the distance to the nearest organism

Because calculating the distance to each object for every particle at every timestep is computationally very costly, the fluid domain is mapped with the distance towards the nearest object. At each cell in the fluid domain, the distance is calculated to all

surface cells of the objects. The minimum of all these distances is the distance to the nearest surface.

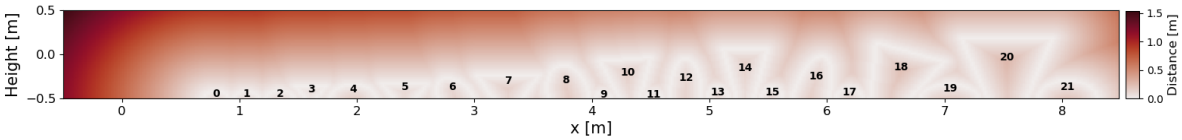

Figure 2.3: The distance to the nearest object in m for the simulation with all 21 objects. The white outlines are the surface cells of the objects. The interaction layers are between 2 and 5 cm from the surfaces.

2.2.3 Voronoi diagram

A voronoi diagram divides the domain into regions of gridcells where a certain object is nearest. This information is combined with the distance map described above to analyse the interaction of particles with each object. The voronoi diagram for the fluid domain is shown in figure 2.4. The algorithm to make it determines for each fluid cell what the distance is to the surfaces of all objects. The object with the minimum distance is mapped to create the voronoi diagram.

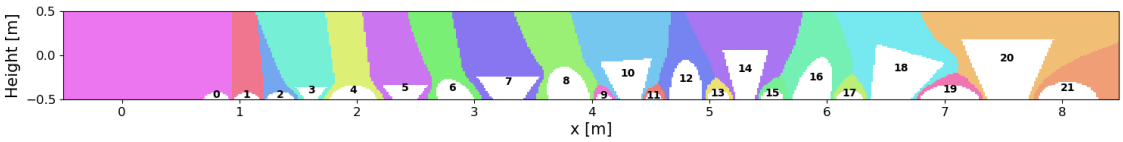

Figure 2.4: The voronoi diagram of the fluid domain. It maps the nearest object to each fluid grid cell. A particle in this thesis interacts with an object when it is the closest object and the distance is smaller than the interaction layer thickness.

2.2.4 Solid-fluid boundaries

By tracing the trajectories of virtual particles in the fluid with the methods described in section 2.3, the discrete velocity field is sampled in continuous space. This necessarily creates problems near the solid-fluid interface as I will elaborate upon in section 2.3.1. To solve the particle motion in the immediate vicinity of this interface, the local orientation of this interface must be known during the particle simulation. For all fluid cells bordering a solid surface, this surface can be in any combination of four directions in this 2D space: up, down, left and/or right. Each direction is given a binary value, True if a solid boundary is present in that direction and False if the cell is bordered by another fluid cell in that direction. By assigning each direction a binary power, the combined direction of boundaries can be captured in a single number. In this study the directions are coupled to the binary powers as follows: 0 = up, 1 = down, 2 = left, 3 = right. For example, if a cell has borders above and to the right the cell is labeled with

$$1 * 2^0 + 0 * 2^1 + 0 * 2^2 + 1 * 2^3 = 9$$

2.3 Lagrangian simulation

The tracking of virtual particles in the fluid is done using Parcels (Lange and van Sebille, 2017; Delandmeter and van Sebille, 2019), a set of Python classes and methods that facilitates the simulation and generates practical output of sets of particles in structured mesh velocity fields. The simulation of these particles calculates the integrated numerical motion of each particle through the fluid domain by interpolating the velocity field in time and space. The Lagrangian (or material) position of each particle is updated every timestep using:

$$X(t + \Delta t) = X(t) + \int_t^{t+\Delta t} v(x(\tau), \tau)\delta\tau \tag{2.1}$$

In this study the integrated velocity is numerically solved using a fourth order Runge-Kutta scheme. The velocity of a particle is entirely given by the interpolated velocity fields described in section 2.3. In some simulations unresolved physics like diffusion or subgrid dispersion by a random walk are added, but in this study these were omitted for the sake of simplicity. To compare the importance of diffusion and advection, the Péclet number was computed, a dimensionless number quantifying the ratio of advection to diffusion:

$$Pe = \frac{LU}{D}, \tag{2.2}$$

in which L is the typical length scale, U is the typical velocity and D is the mass diffusivity. Since in many parts of the domain the velocities $\mathcal{O}(1\,\mathrm{m\,s^{-1}})$ are very much larger than the mass diffusivity $\mathcal{O}(10^{-8}\,\mathrm{m^2\,s^{-1}})$, diffusion is assumed to be negligible at all but the smallest scales. Near the solid-fluid boundaries where both the velocities and length scales become very small, diffusion becomes important. That is why the uptake of solutes by the sedentary organisms is through a diffusive boundary layer of $\mathcal{O}(1\,\mathrm{mm})$. To fully resolve the pathways of solutes to the organisms, these diffusive and dispersive processes must be added.

The velocity fields and the maps generated in preprocessing are loaded as input for the particle simulation in what is called a fieldset. The advection based processes that can be studied within an open fluid domain can be separated in two types: advection of water entering the domain from an open boundary and advection between certain regions within the domain. To quantify these two types of fluxes, two types of particle simulations are run. The first repeatedly releases particles at the upstream open boundary at the left-hand side of the domain. With this the influx of water into the local reef canopy can be quantified. A second simulation tracks a single release of particles at all gridcells within the domain. This simulation is used to quantify the connection between the different objects in the domain.

During the simulation, the particles sample the distance map, the voronoi diagram and the map of the local solid boundaries. Whereas the interpolation of the velocities is bilinear in space to increase accuracy, these maps cannot be correctly interpolated bilinearly for several different reasons. The distances to the nearest surface are not bilinear, while interpolating the voronoi diagram and the binary combinations of boundary directions makes no sense. These quantities are therefore

sampled by nearest neighbour interpolation, which fixes the resolution at the grid scale.

The particle tracking simulation calculates the particle positions with a timestep of 0.001 seconds and outputs their location every 0.1 seconds. The particles released at the left-hand boundary are released every 0.1 seconds. The total runtime of the simulation is 60 seconds.

2.3.1 Boundary conditions

As the particle locations are determined by interpolating the discrete velocity fields, the trajectories are drawn in a continuum: instead of particles simply jumping from discrete gridcell to discrete gridcell, particles find themselves in a specific location relative to the points at which the velocity is known. By using Runge-Kutta integration, the trajectories become very accurate when there are little unresolved or unparameterized physics. In fluid cells bordering a solid boundary however, the unresolved physics within a cell that make the model satisfy the boundary conditions are aggregated in the discrete velocity. As concisely formulated in the book Particles in the Coastal Ocean by Lynch et al. (2014): 'Particles immersed in continuous velocity fields will necessarily risk collision with kinked model boundaries.' The word 'kinked' in this quote refers to the discrete gridcells of solid objects that have 90° corners in the structured mesh. This problem requires researchers to define the boundary conditions for the particles that are studied. Relatively little consensus is available within the modelling community on how to define these boundary conditions. At an ocean scale particles may end up on beaches, but at the scale of this study and assuming that the particles studied here do not enter organisms due to their velocity coming into this boundary, we have defined a novel parameterisation that repels particles from the boundary by restricting the motion normal to the boundary as it gets closer.

A-grid boundaries

The velocity fields generated by Gerris are structured in an Arakawa A-grid (Arakawa and Lamb, 1977). The A-grid is an unstaggered grid where all variables are defined at each node. In an A-grid cell velocities are computed at either the center or the corner of the cell. Gerris uses an algorithm to divide the space into cells and outputs the velocities at the center of the cells as they are defined by the geometry of the solid objects. The interpolation scheme in Parcels interpolates between the output, which means the scheme does not recognise the boundaries correctly, as shown in figure 2.5a: interpolating between the fluid cell and the solid cell means the velocity only goes to zero at the center of the solid cell, not halfway between the two, where it is supposed to go to zero. If Parcels simulates a set of particles in this domain without changing the interpolation, some particles will enter the solid cells and either get stuck between four solid cells or move out of the solid cells again when the velocity in the surrounding fluid cells becomes away from the local boundary. To draw more accurate trajectories around the objects, the interpolation in this part

of the domain must be adapted.

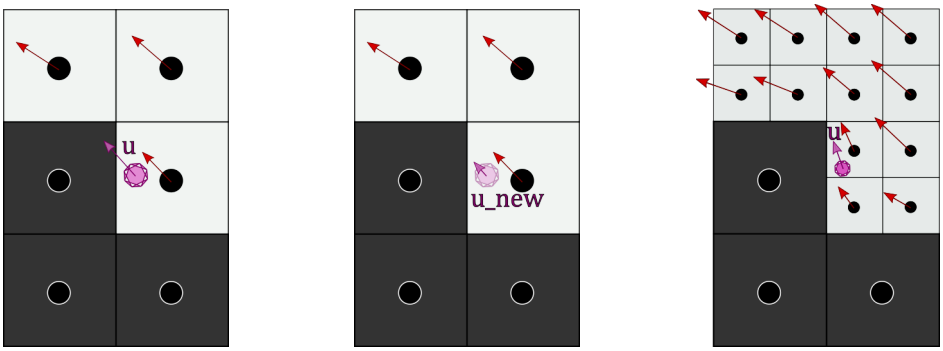

(a) Particle velocity interpolating fluid and solid cells

(b) Interpolating correctly to the solid-fluid boundary

(c) Anisotropy within a fluid cell emerges from higher resolution

Figure 2.5: Tracing trajectories near the solid-fluid boundary. The particle velocities in purple show why the boundary conditions must defined for the particles. Solid cells in black and fluid cells in light-gray. The velocity data as the red arrows are bilinearly interpolated by Parcels.

Interpolation

The velocities are reduced to zero at the boundary by evaluating the position of the particle in the cell relative to the boundary. Since the orientation of the solid-fluid interface is known for each cell from the map with binary combinations described in 2.2.4, the distance to that interface can be inferred from the position of the particle within that cell. The particle velocity can then be made a function of the distance towards the boundary. If this is a linear function, the velocities are essentially interpolated as in the rest of the fluid but now to the correct location of the boundary. An example of what that would look like is shown in figure 2.5b. This solution improves the realism of the trajectories but leaves the problem with the kinked boundaries untreated: the particle in figure 2.5b is still on its way to get stuck on the boundary.

Subgrid Anisotropy

The reason the particle in figure 2.5c will still get stuck is that within a cell, at the subgrid scale, the fluid velocity is anisotropic: if you look at the fluid velocities in more detail, at a higher resolution, the fluid approaching the wall moves more tangentially to the solid-fluid boundary (figure 2.5c). Increasing the resolution of the model thus improves the accuracy of the trajectories. The problem remains at a smaller scale however as the particle in figure 2.5c admittedly moves more tangentially with respect to the boundary, yet still retains a component normal to the boundary. In the limit towards the boundary, both the tangential (u_t) and the normal (u_n) components of the velocity must go to zero and to parameterise the subgrid anisotropy the ratio of the tangential and the normal component must go to infinity (figure 2.7). To solve the latter condition, the derivative of the normal

component must also be zero:

$$u_t(0) = 0$$
$$u_n(0) = 0$$
$$\frac{du_n}{dn} = 0$$

The first conditions are solved by interpolating correctly to the boundary. To solve the last condition, the normal velocity can be interpolated with a parabolic profile as a function of the distance to the wall: the simplest profile with a zero derivative (see figures 2.7a and 2.7b).

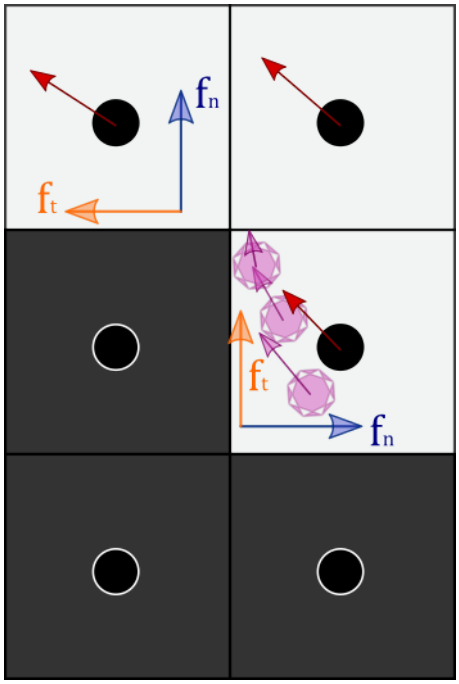

Figure 2.6: Boundary condition separating normal and tangential velocity components. The purple particle shows how the velocity of the particle becomes smaller and more tangential as it moves towards the boundary. Because the local orientation of the solid-fluid boundaries is known from preprocessing, the normal and tangential direction of the nearest boundary can be used to define the profiles shown in figure 2.7. The local normal and tangential direction w.r.t the nearest boundary are shown by f_n and f_t respectively. The velocity output by the CFD is shown with the red arrows.

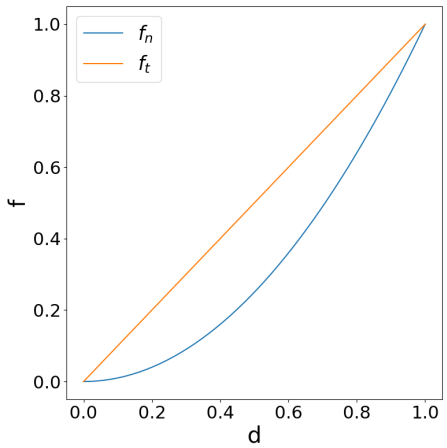

(a) Tangential and normal profiles

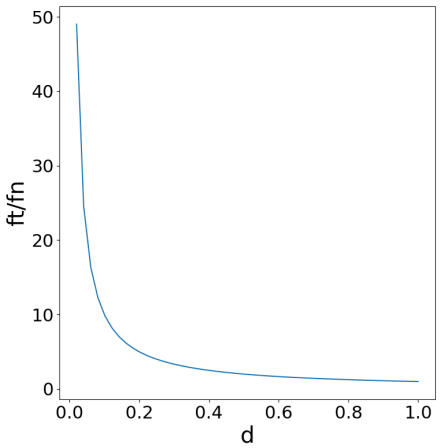

(b) Ratio of tangential and normal profiles

Figure 2.7: The normal and tangential profiles as a function of distance to the solid-fluid boundary d.

CFD condition

The boundary conditions are defined to trace more accurate trajectories near the solid-fluid boundaries and to be able to trace them continuously from object to object. The implementation of the interpolation scheme described above is only valid when a particle satisfies the Courant-Friedrichs-Lewy condition for explicit integration methods:

$$C = \frac{u\Delta t}{\Delta x} \leq 1 \tag{2.3}$$

This condition states that information that travels with a speed u may not travel a distance more than Δx within one timestep Δt. For the parabolic boundary profile to effectively trace trajectories tangentially to the boundary, Δx is much smaller than the model Δx of 0.015625 m. The appropriate Δt found experimentally to bring down the number of particles crossing the solid-fluid boundary to zero was 0.001 s. Then the timestep is sufficiently small to resolve the subgrid anisotropy in such a way that the normal component of the velocity does not carry any particles across the boundary. A figure detailing the amount of stuck particles with different boundary conditions is included in the appendix A.1.

2.4 Postprocessing

After simulating the particle trajectories, the trajectory data are postprocessed to generate the volume flux data and the network to be analysed in the results. The volume fluxes are calculated from the particles released at the edge of the domain by the functions *VolumeFluxesPerarea* and *TotalVolumeFlux* in the functions script provided at github.com/OceanParcels/CoralDispersion.

The 2D volume for each particle is calculated by:

$$u_0 * dy * dt[m^2]$$

Here u_0 is the velocity of the particle as it is released. The volume flux is the sum of the particle volumes divided by the timespan over which particles were released and the surface length in m of the respective objects. The first function saves the volume flux of particles to the first object they interact with. First it selects the particles that pass through any interaction layer. Then it finds the first instance it comes within the interaction layer thickness (2.3) and assigns the volume of the particle to the object it is closest to (2.2.3). The second function calculates the total number of particles that reach every object. It does so by finding all particles that enter any interaction layer, then taking the sum of all the particles volumes for each object.

The network is defined by the particles that travel through two consecutive interaction layers. It is a directed network, which means that the connection (edge) between two objects (nodes) is defined separately for both directions. In practice this means that the edge from an object to another object downstream is stronger than from that object downstream to the object upstream. Edge strength implies

that the network is weighted: Not all edges are equally strong. The strength of the edge is determined by the number of particles per number of simulated seconds per surface length of the receiving object. Because the objects are 2D, the surface has a length and not an area. It is defined in this way to capture a chance of uptake by the receiving object, which usually depends on the surface area. A particle counts towards an edge if it passes through two interaction layers in the respective order. The adjacency matrix containing all the edges and their strength is calculated by the function *AdjacencyMatrixPerarea*. Each edge is calculated by comparing all combinations of objects in both directions and checking for each particle in the starting objects interaction layer if it enters the other objects interaction layer at a later moment.

Chapter 3

Results

The transport processes that can be studied within an open fluid domain were separated in two types: advection of water entering the domain from an open boundary and advection between certain regions within the domain. Unless specified otherwise, the figures in this section are from simulations with a parabolic vertical velocity profile, wave velocities imposed at the upper boundary, a parabolic velocity profile normal to object boundaries and a boundary layer thickness of 5 cm.

3.1 Influx

The influx of virtual particles from the left-hand side of the domain is analysed in this section. It focuses on three main patterns: the integrated trajectories of the particles that interact with the solid objects, the height distribution of those particles when they enter the domain, and the volume flux towards each object.

3.1.1 Trajectories

The trajectories that are calculated by simulating virtual particles can be animated or traced out entirely to show their integrated motion over time. By color-coding the trajectories based on their destination, patterns in the pathways of the dynamical system become visible. Figure 3.1 shows the pathways of all particles released at the left-hand boundary of the domain that come within 5 cm of any solid object. Their colors correspond to the first object of which they cross this threshold. All trajectories that interact with the solid objects are confined to the lower part of the domain. Remember that the vertical velocity is prescribed to be zero at the upper boundary. This restricts vertical movement in the upper part of the domain and thus prohibits entrainment of water towards the bottom. Also, the 2D nature of the domain prevents horizontal divergence in the canopy to allow for vertical movements. At the same time, the 2D nature forces water blocked by a solid object to return in an eddy instead of passing around the object horizontally.

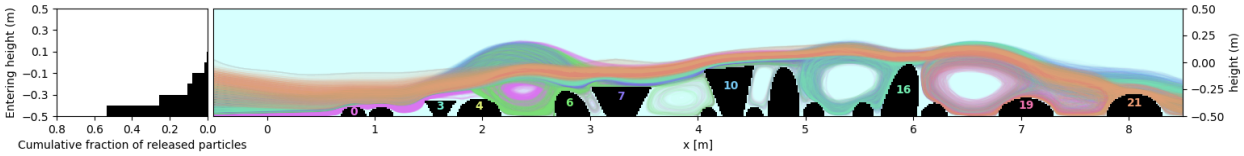

(a) Flow: Parabolic + Waves Boundary Condition: parabolic-linear Boundary Layer Thickness: 5 cm

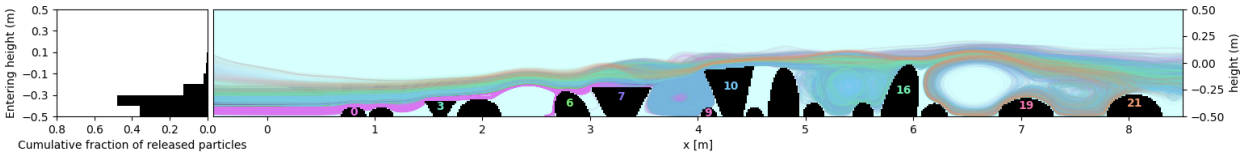

(b) Flow: Parabolic Boundary Condition: parabolic-linear Boundary Layer Thickness: 5 cm

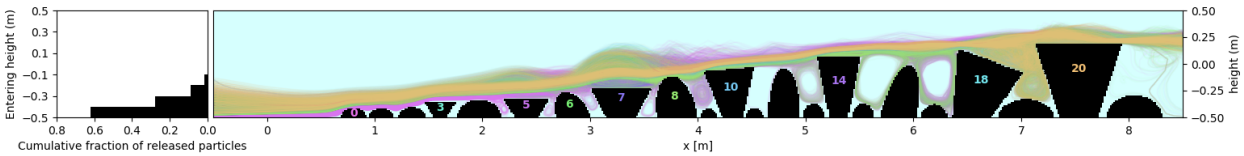

(c) Flow: Parabolic + Waves Boundary Condition: parabolic-linear Boundary Layer Thickness: 5 cm

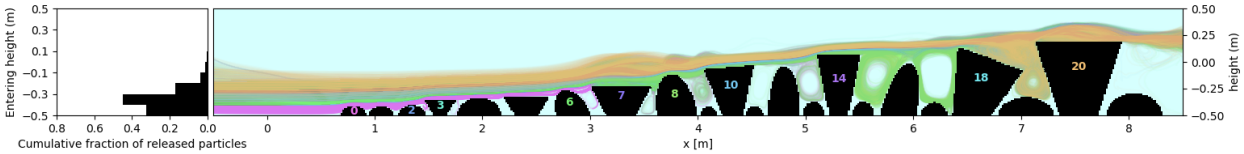

(d) Flow: Parabolic Boundary Condition: parabolic-linear Boundary Layer Thickness: 5 cm

Figure 3.1: Trajectories of incoming particles. Each figure shows the trajectories of the virtual particles released at the left-hand boundary. The objects are numbered in a color which corresponds to the color of the trajectories that end up within their boundary layer of 5 cm first. This means that the objects that do not have any particles entering their boundary layer first are not numbered. Also, the trajectories of virtual particles that do not enter any boundary layer are not drawn. The trajectories are drawn in the order of their corresponding objects: those to object 0 are drawn first and all other trajectories overlap until object 21 is drawn on top. The horizontal barplot on the left shows the distribution of the release height for all drawn trajectories. Figures a and b show the trajectories with 16 objects with and without waves respectively. Figures c and d have all 21 objects and show the simulations with and without waves respectively again.

Comparing figures 3.1a and 3.1b with figures 3.1c and 3.1d shows the effect of the object spacing on the pathways. Increased spacing allows larger clockwise eddies to form in the wake of the objects. As the horizontal extent of the eddies increases, so does the vertical extent. The larger vertical extent of the eddies can clearly be observed in figure 3.1a at x = 2-3m, x = 5-6m and x = 6-7m. Since no diffusion is present in the particle simulations, these larger eddies only contain particles from the lower part of the domain and do not enable net vertical transport of particles. This can be concluded by observing that the trajectories in the eddy all follow both the upward and the downward motion. No particles from higher up are carried only by the downward motion and no particles from near the bottom are carried only by the upward motion and thereby escape the canopy layer. To determine transport pathways for oxygen for example, this observation demonstrates why adding diffusion is very important in turbulent flows, even when advection is very dominant over diffusion. Small differences in position can lead to drastically different pathways in

a turbulent field.

What is clear from the animation of figure 3.1a is that the large eddy between 2-3m plays an important role in the transport of the red and orange particles corresponding to objects 19 and 21. While the eddy displaces pink, yellow, green and dark blue particles that end up entering the boundary layers of objects 0, 4, 6 and 7, the breaking of the eddy is always followed by the transport of particles higher in the water column towards objects 19 and 21, as seen from the red and orange lines that move downwards directly from the start of the domain and do not enter the eddy because by that time it has broken up. In this way water from higher in the water column is advected towards the objects, which can also be seen by comparing the height distributions in figures 3.1a and 3.1c. This is done in figure 3.2a. Where the spacing is larger, water from higher in the water column reaches objects more often. Interestingly, this effect only arises in the presence of waves. The waves interact with the eddies that form in the wake presented by the larger spacing.

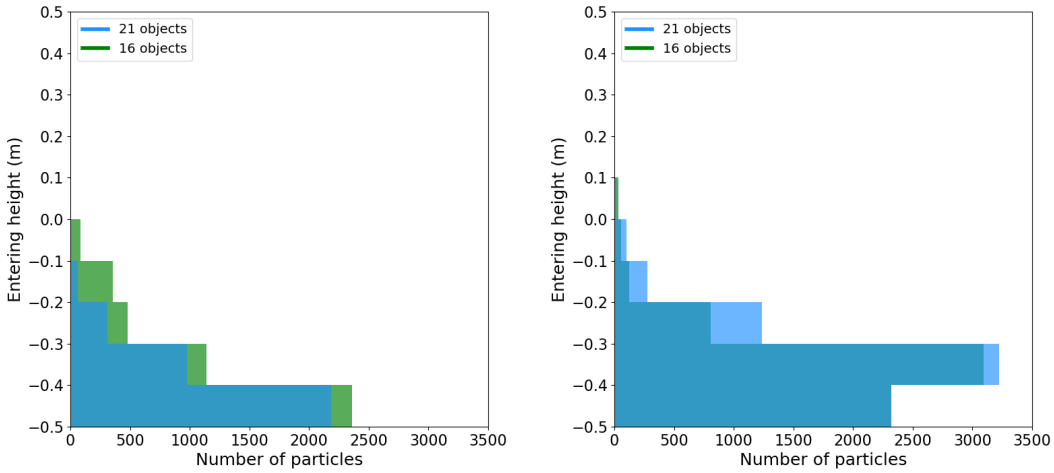

(a)
Flow: Parabolic + Waves
Boundary Condition: parabolic-linear
Boundary Layer Thickness: 5 cm

(b)
Flow: Parabolic
Boundary Condition: parabolic-linear
Boundary Layer Thickness: 5 cm

Figure 3.2: Height distribution of the incoming particles that reach the boundary layer of each object. The same distributions as seen in the figures to the left of the trajectories in figure 3.1, but in absolute numbers of particles. The simulations with different numbers of objects are plotted over each other.

The particles entrained from higher up in the water column in the way described in the previous paragraph are all particles that end up at objects 19 and 21. The water closer to the bottom naturally enters the boundary layers of the upstream objects before possibly entering the boundary layers of objects further downstream. Because the trajectories reaching the furthest objects are drawn last, it appears the volume flux is quite evenly distributed over the objects, but figures 3.3 and 3.4 show the vast majority of the incoming volume flux interacts with object 0 first. Only particles that start higher up in the water column manage to make it past some objects before entering the canopy. Knowledge about these transport scales can

inform scientists measuring vertical profiles what the horizontal scale of influence is at each height. If one were to measure a vertical profile to study these 9 meters of the seafloor, these simulations suggest that it one should measure up to 0.5 m from the bottom on the upstream end. Here it is important to note how simplistic these pathways are by only looking at the first object water particles encounter.

3.1.2 Incoming volume flux

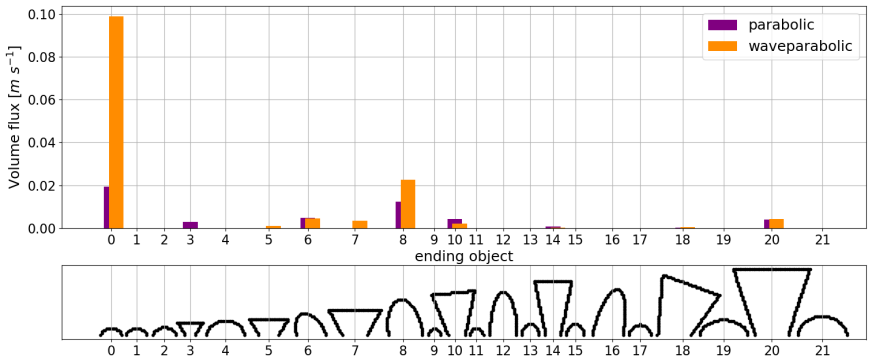

(a) Boundary Condition: parabolic-linear Boundary Layer Thickness: 5 cm

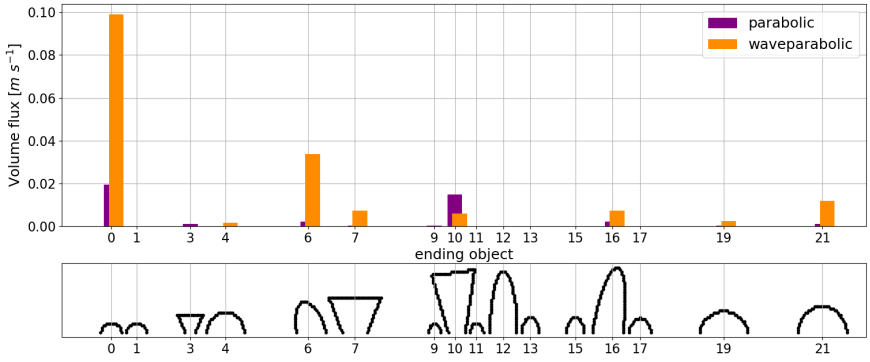

(b) Boundary Condition: parabolic-linear Boundary Layer Thickness: 5 cm

Figure 3.3: The effect of waves on the 2D volume flux of water to the first object it enters the boundary layer of. This is the volume flux corresponding to the trajetories drawn in figure 3.1. The volume for each particle is calculated by u_0 * dy * dt $[m^2]$. The volume flux is the sum of the particle volumes divided by the timespan over which particles were released and the surface length in m of the respective objects.

Figure 3.3 shows how the simulations with waves allow very little water from the left-hand boundary to reach any objects other than object 0. This indicates how difficult it is to learn the entrainment mechanisms from figure 3.1a. The trajectories are drawn over the top of one another and the amount of lines and the volume they represent is not visible. By animating the particle trajectories, the volume distribution becomes more noticeable as the particles interacting with object 0 are released continuously, while the particles that interact with other objects are only released periodically. Based on these volume fluxes and the height distributions predictions can be made regarding the probability that measured quantities interact

with the objects downstream. In models with the exact seafloor and boundary conditions from observations these predictions can become very specific, but by parameterising the seafloor topography one can also make more general estimates.

Apart from advecting many more particles to object 0, the effect of the waves seems to be to increase the volume flux towards all the objects. Again especially the combination of waves and increased spacing seems to have the strongest effect. I hypothesize that this general increase in volume flux results from the eddies causing a larger fraction of the water column to interact with the objects. Since the water from higher up in the water column has a larger velocity, the volume sampled by particles released with the same frequency is larger. The positive momentum transfer down towards the objects causes more water to flow past the objects.

Figure 3.4 shows the effect of the object spacing on the volume flux towards each object. The dominant effect is quite simple: when a large object is removed the first object in the downstream direction now encounters the water that would otherwise have been diverted by the removed object. This can be seen at the green bars for objects 6, 10, 16 and 21.

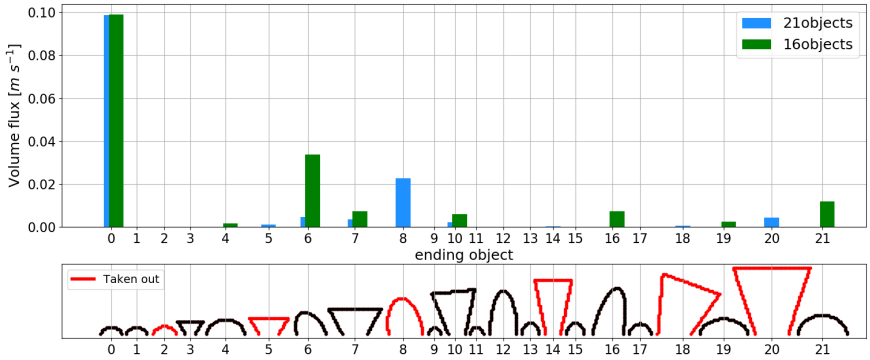

(a) Flow: Parabolic + Waves Boundary Condition: parabolic-linear Boundary Layer Thickness: 5 cm

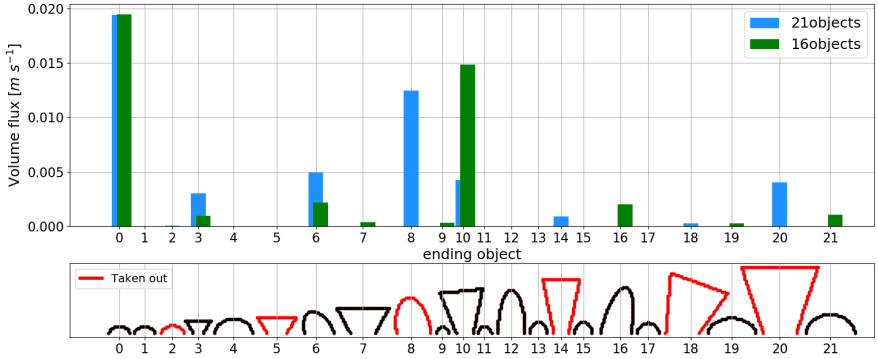

(b) Flow: Parabolic Boundary Condition: parabolic-linear Boundary Layer Thickness: 5 cm

Figure 3.4: The effect of object spacing on the 2D volume flux of water to the first object it enters the boundary layer of. This is the volume flux corresponding to the trajetories drawn in figure 3.1. The volume for each particle is calculated by u_0 * dy * dt $[m^2]$. The volume flux is the sum of the particle volumes divided by the timespan over which particles were released and the surface length in m of the respective objects.

Because of this dominant effect, it is hard to observe any other effects. Looking at all the objects in each figure, the total area of the green bars is larger in 3.4a while the area of light blue bars appears larger in 3.4b. This reinforces the idea that a wider spacing is effective in increasing the volume flux when waves are present (green bars in 3.4a) and not very effective in areas with little waves (light blue bars in 3.4b). However, this observation is complicated by the fact that these volume fluxes are calculated as a function of surface length, which means that if the same volume of water interacts with a smaller object because the larger objects are taken out, the volume flux per surface length will increase. This means that the focus in this figure is on the object conditions rather than the distribution of the incoming volume. Similar figures with the results not as a function of the receiving objects surface length are included in the appendix.

With a boundary layer thickness of 5 cm, it seems as if the smaller objects like 9, 11, 13, 15 and 17 do not receive any of the water flowing into the domain in 60 seconds. Remember however, this volume flux assumes that once water has entered a boundary layer, its characteristics are so significantly altered that it is unable to be traced back to where they entered the domain. This depends significantly on the specific process to be studied, on the exact distance to the organism surface and to the time spent in the boundary layer, which are not taken into account here. Figure 3.5 shows how much of the incoming water reaches each object at any point in the simulation.

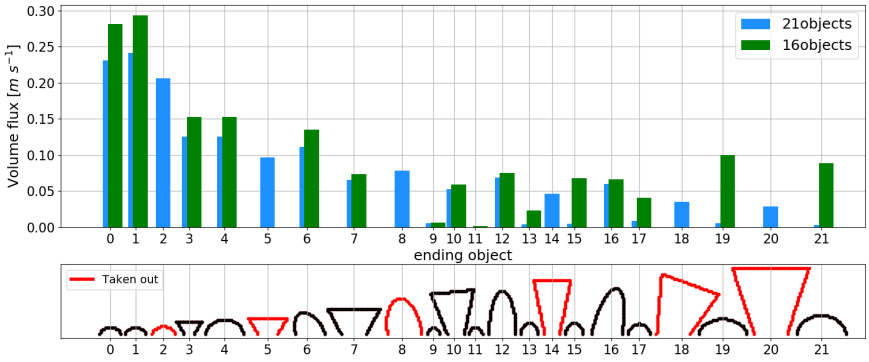

(a) Flow: Parabolic + Waves Boundary Condition: parabolic-linear Boundary Layer Thickness: 5 cm

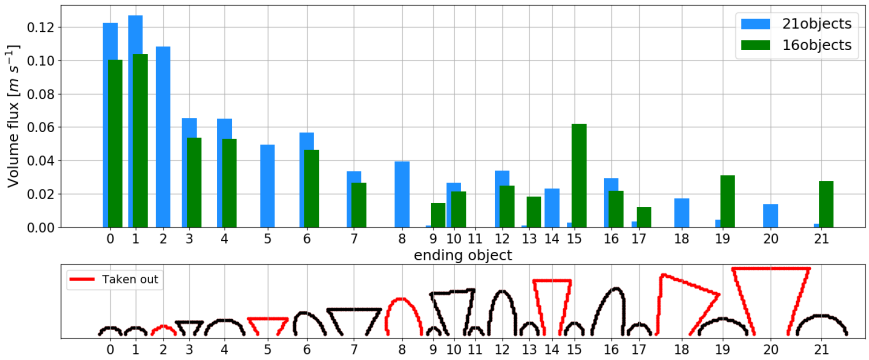

(b) Flow: Parabolic Boundary Condition: parabolic-linear Boundary Layer Thickness: 5 cm

Figure 3.5: Total volume flux per object surface length that enters the boundary layer at any time. If a particle travels through two consecutive boundary layers, it counts towards the volume flux to both objects. The volume for each particle is calculated by u_0 * dy * dt [m^2]. The volume flux is the sum of the particle volumes divided by the timespan over which particles were released and the surface length in m of the respective objects.

This can be used to estimate at what timescales the water around an object is refreshed. A simple measure for residence time is:

$$\tau = \frac{V}{f} = \frac{hL_{surface}}{f} \tag{3.1}$$

In which V in this case is the 2-dimensional volume of the boundary layer, which is the boundary layer thickness h times the length of the 1-dimensional surface of each object and f is the total volume flux into the volume V. Since these fluxes (figure 3.5) are calculated as a function of this surface length h, the residence times are simply h over the values plotted in figure 3.5. This shows how the residence time of water advected from the left-hand boundary is affected by changes in object spacing and waves.

When waves are present, an increased spacing between the objects has a positive effect for the total volume fluxes to the remaining objects, decreasing the residence time of water in the interaction layers around these objects. When waves are not present the opposite is true for almost all objects.

3.2 Sedentary Organism Connectivity

To study the local spread of metabolites, larvae, and changes in local oxygen and nutrient conditions, we define a network as described in the postprocessing section of the methods.

3.2.1 Networks

The adjacency matrices of the network of objects are shown in figure 3.6. Adjacency matrices show the strengths of the connections, called edges between all objects. A simple flow in a small domain already results in a complex pattern because 21 objects have 441 possible links. Almost all connections are located in the lower right triangle of the matrix because these are the ending objects that are downstream of the starting objects. The diagonal is set to zero as this definition of the adjacency matrix would count all particles that stay in the boundary layer for more than one timestep towards the strength of the link, which is all particles in practice. Although it may be interesting to look at these so-called self-edges in some networks of this kind, here they are excluded.

The edges above the diagonal indicate the instances where particles travel against the main flow direction. This occurs at the bottom between objects as flow separation induces flow reversal along solid boundaries. This flow separation occurs at all objects except for objects 0 and 1. In most cases the reversed flow direction extends only to the direct neighbour in the upstream direction. When a number of smaller objects are in between two larger objects however, this return flow can extend past multiple objects, which shows up as a larger block of edges above the diagonal. In the simulation with all objects (figure 3.6a) this occurs for one extra object over objects 9, 11, 13 and 19, all single smaller objects between two larger ones. Interestingly, object 16 is small enough to allow for a return flow from object 18 all the way back to object 14. In the simulation with removed objects the absence of larger objects allows larger wakes to carry particles further back against the main current, especially between objects 16 and 10.

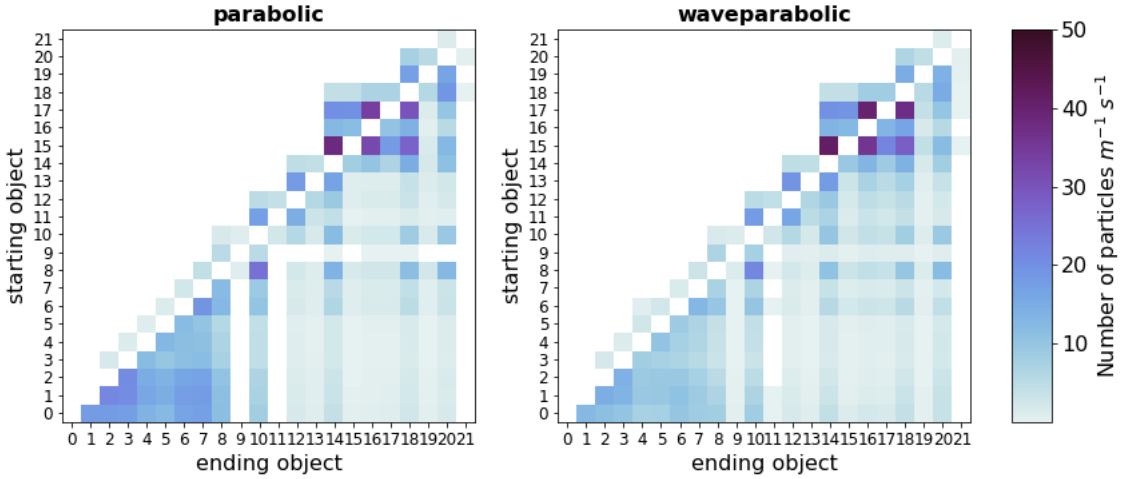

(a) Organism network for the simulation with 21 objects

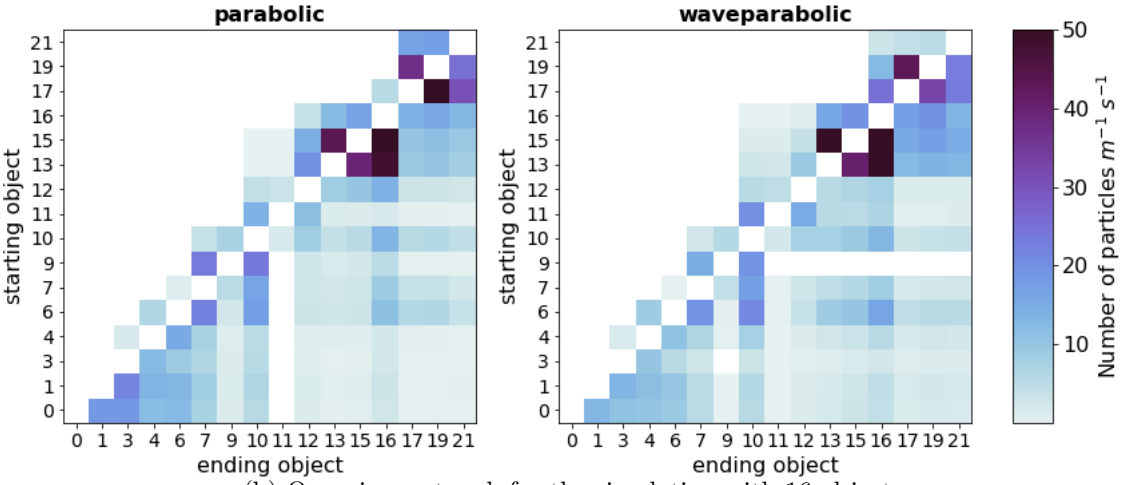

(b) Organism network for the simulation with 16 objects

Figure 3.6: Adjacency matrices show the weighted directed edges between all combinations of objects. When no particles connect two objects the edge is completely white. The self-edges located at the diagonal are all set to zero.

To develop an understanding of the length scales at which local connectivity is important, we can focus on the steepness with which the edge strength decrease in the downstream direction. If the edge strength of an object decreases quickly with distance downstream, its influence is mainly local. If many particles stay within the canopy layer and travel steadily downstream, the edges will hardly decrease in strength and the length scales of connectivity may become very large. By studying the connectivity of individual objects, the length scale of influence of a single object can be revealed. Note that in a 3D reef domain this length scale necessarily depends on time and the 2D horizontal directions, the latter of which is not included in this study. In this simulation of 60 seconds, the length scale of connectivity is strongly related to the distance between large objects or the distance between the domain boundary and large objects. Especially in figure 3.6a, the block of edges between object 0 and 8 all have a similar strength, whereas the edges between those objects and even the larger objects like 14, 18 and 20 decreases quickly. This means that the main length scale of connectivity at a timescale of 60 seconds for object 0 is about

the distance between it and object 8/object 10, around 3 m. Now this conclusion in itself is not very interesting or robust, given the arbitrary selection of objects and the 2D flow, but looking at the effect of waves on the connectivity reveals an interesting pattern. Figure 3.7 shows the difference between the adjacency matrices with and without waves. Figure 3.7a clearly shows the waves decrease the edge strength of the objects connected by a more unidirectional, more laminar flow (objects 0 to 7) and increase the connectivity of objects connected by eddies in object wakes, thereby effectively increasing the length scale of connectivity for objects 0 to 7. This can be seen in figure 3.6a where the edge strength decreases less abruptly when waves are present.

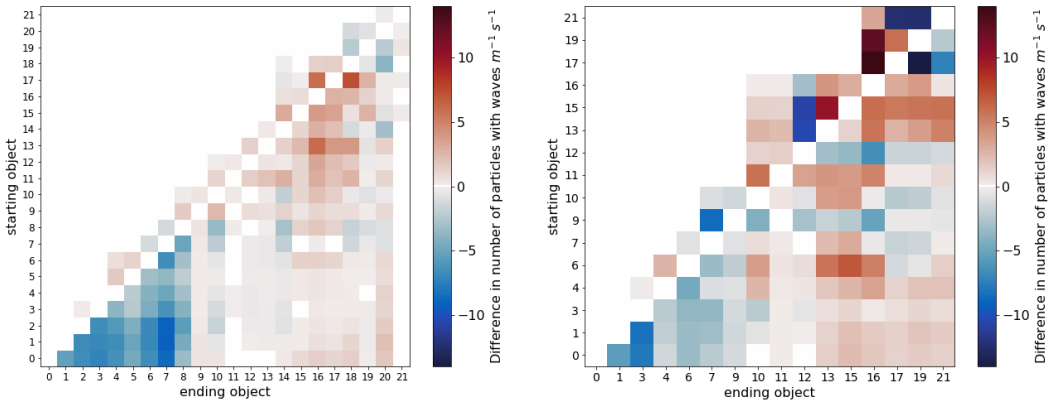

(a) All objects (b) Removed objects

Figure 3.7: Effect of waves on adjacency matrices. Red (blue) edges increase (decrease) in strength when waves are added.

Another interesting observation in figure 3.7a is the positive effect of waves on the edges above the diagonal: waves tend to enhance the eddies between objects, increasing the transport of water against the main flow direction. The effects of waves on both the length scale and the return flow are less pronounced in the simulations with removed objects.

Figure 3.8 shows the effect of the removal of the objects on the adjacency matrices. Since the network with all objects and the network with objects removed have a different shape, the difference matrices are depicted in two ways. In a) the matrix shows the edges of all objects, with the edges for all removed objects hatched. Since these objects do not have any edge in the simulation with removed objects, the effect of removing the objects is necessarily negative for these edges. In b) the matrix shows only the objects that are present in both simulations. The main observation is that the edges that are lost by the removal of the objects are compensated by an increase in the remaining edges. In 3.8a the red increases are alternated with hatched blue decreases. The edges between the remaining objects in 3.8b have but for a few all increased in strength. This means that the remaining objects are better connected to the other remaining objects, but the net effect of removal on the individual condition of each object is hard to determine from these difference matrices. How does the loss of connectivity due to the removed edges

weigh against the increased strength of the remaining edges? This can be studied by analysing each column in the matrices.

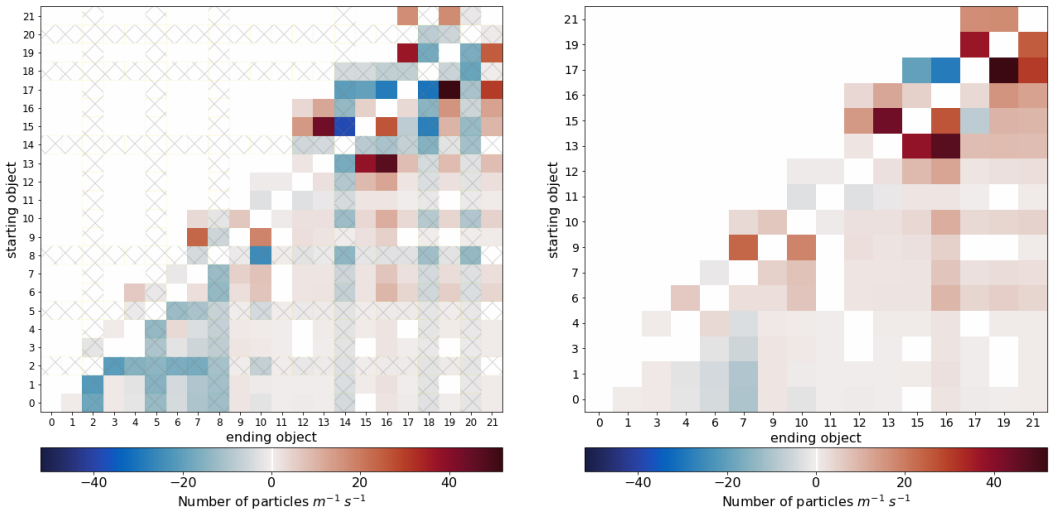

(a) All 21 objects (b) 16 objects present in both simulations

Figure 3.8: Effect of spacing on the adjacency matrices for a flow with waves. Since the two matrices do not have the same amount of nodes due to the removal of the objects, there are two ways to show the difference: in a) all objects are included with edges that disappear hatched. In b) only the remaining nodes and edges are shown

The columns in the adjacency matrices (figure 3.6) that catch the eye by their darker colour represent the larger objects that receive particles from many upstream objects that all have to be forced over these larger objects. Examples of this are objects 10, 14, 18 and 20 in figure 3.6a and objects 10 and 16 in figure 3.6b. Conversely, the columns of ending objects 9, 11 and 21 in figure 3.6a catch the eye because many of the objects do not have any particles that end up in their boundary layer. The column-sum of these adjacency matrices is called the indegree. This is a simple measure for the how connected an object is to all surrounding objects. The indegree of all objects can be analysed from figures 3.9, 3.10a and 3.10b. Figure 3.9 shows the effects of spacing on the indegree. It shows especially how removing objects 14, 18 and 20 greatly increases the connectivity of all objects in the direct vicinity. This answers the question of the net effect of spacing on the remaining objects. In an area with little variation in the vertical extent of the objects, removing every third object has a slight net negative effect on the indegree of each object. Being in the upstream part of the domain means the number of objects contibuting to each objects indegree is small, making the differences small as well. In the downstream part of the domain with a lot of variation in the vertical extent of the objects, removing some of the larger objects has a large net positive effect on almost all remaining objects, even though they lose the particles that connected the boundary layers of the removed objects to theirs. The larger spacing between large objects in this 2D domain allows larger eddies to carry more particles at higher velocities past these smaller objects. This suggests that the death or removal of some larger organisms in a dense coral community may greatly increase the flow towards the remaining

(smaller) organisms.

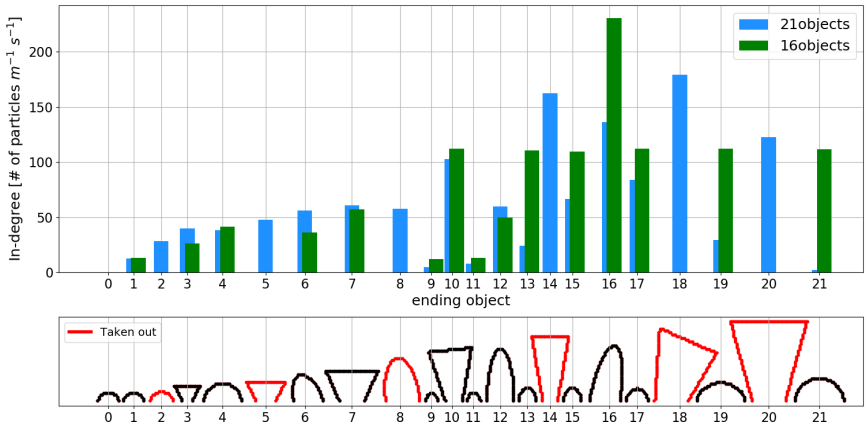

Figure 3.9: The indegree or column-sum of the adjacency matrices shows how the receiving objects are affected by the removal of the objects.

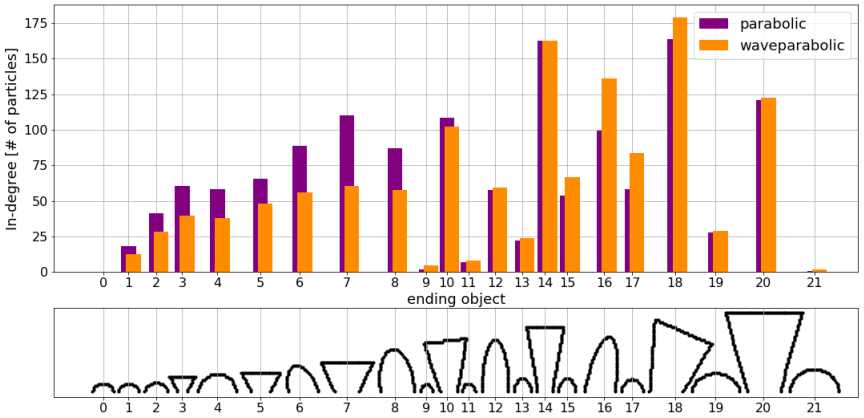

(a) Indegree object spacing comparison.

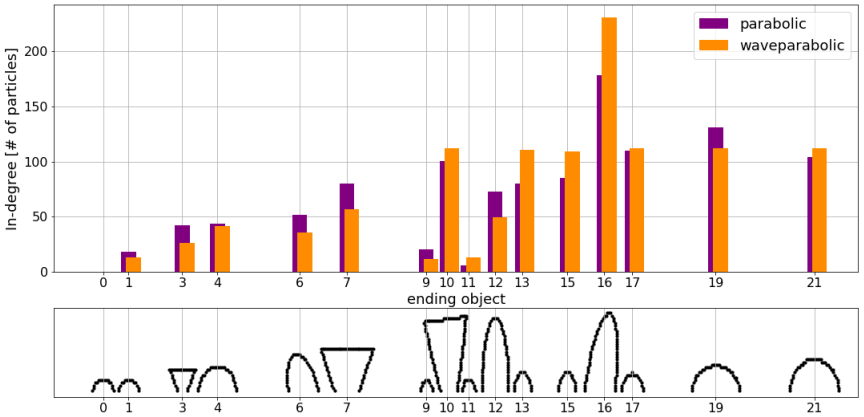

(b) Indegree object spacing comparison.

Figure 3.10: Effect of waves on the indegree

The effect of waves on the indegree of objects, shown in figure 3.10, is similar to the effect of removing a number of objects. It is more consistent over the entire domain, since removing objects changes the flow in specific places while adding waves changes the flow everywhere and the effect is less drastic in some places for the same reason, but it tends to decrease the indegree where objects have little variation in vertical extent and increase the indegree where neighbouring objects have a large variation in vertical extent. The results from the indegree agree with the results from the difference matrix (figure 3.7) and the incoming volume flux (figure 3.3). The waves increase the number of particles in the eddies in the wake of larger objects and generate vertical movement over the objects in the upstream part of the domain that inhibit particles from travelling through all consecutive boundary layers, thereby increasing the distance particles travel before they interact with another object.

Chapter 4

General Discussion and Recommendations

The three main caveats to the interpretation of the Lagrangian analysis in this thesis concern the boundary condition parameterisation, the smallest scale motions and the 2-dimensionality of the domain. The boundary condition parameterisation successfully managed to repel particles from the solid-fluid boundary, which allows the particle trajectories to be tracked through the interaction layers of objects. The parameterisation is has not been validated however by observations or models with a higher resolution. This would be necessary to examine whether the trajectories here are traced accurately.

The subgrid turbulence in the data is represented by a bulk viscosity parameterisation. This is not the most sophisticated turbulence model and therefore might not capture the flow conditions accurately, especially since the roughness elements in the flow might generate turbulent conditions. The other shortcoming regarding the subgrid motion is that it is not included in the Lagrangian displacement (equation 2.1). By adding a random walk to the particle motion, the subgrid motions from turbulence and diffusion can be included.

Finally, the 2-dimensionality of the domain may severely qualify the results. Adding an extra dimension may significantly reduce the low pressure region in the wake of organisms because flow in the third dimension can readjust to neutralize the pressure anomaly. This would have significant influence on the pathways entraining water into the reef canopy.

The results suggest that the organism spacing interacts with the waves to create larger eddies. Modelling studies can further describe the wave-current interactions in these types of domains (van Rooijen et al., 2020; Lowe et al., 2008) and their consequences for Lagrangian transport. Observations of reefs exposed to different wave conditions can complement the long-term consequences of these results to the reef ecosystem response to anthropogenic forcings.

The analysis techniques described in this study could be applied to more sophisticated models and experimental model setups. The development of photogrammetric models of the seafloor (Leon et al., 2015; Burns et al., 2015) opens possibilities in

high detail modelling and monitoring of specific reef environments around the world. The techniques used here can be applied in the new models to extend the analysis of the hydrodynamic conditions in these environments.

Conversely, simplifying the model domain can be insightful to generalize the effects of specific geometric characteristics. In this thesis the effects of organism spacing and waves are quantified, but a more rigorous model setup can further characterise specific regimes. Geometric properties like spacing, size and size variation can be compared to wave amplitude and period as in Yu et al. (2018).

Here the length scales of interaction within 60 seconds are studied in a domain of a 9 m long seabed. Sedentary organisms exhibit behavioural patterns on tidal and diurnal timescales (LASKER, 1979; Levy et al., 2006). To study the influence of changes in an organism at this scale, the simulation must be extended in time but therefore also in space. In practice this extension of the spatial dimensions comes at the price of topographic details. The transport processes quantified in this thesis may be used to parameterise boundary layer transport in the study of transport phenomena studied at a larger scale.

To improve the methods used here, efforts might be directed towards developing a better way to quantify interaction of particles with the sedentary objects. The interaction layer of a number of centimeters is a very rough estimate of how likely particles are to interact with organisms. Probabilistic interactions could be implemented and the contribution of each particle to the edge strength should probably depend on the time spent in the interaction layer. If a specific advective process is studied, more detailed behaviour of active interaction could be modelled.

Increasing realism in the interaction of pelagic particles with the sedentary organisms may reveal more complex preferential pathways for the particles. Sponges are thought to play an important role in the nutrient recycling within an ecosystem de Goeij et al. (2013), partially because their bodies are porous, which enables large uptake and efflux rates (Larsen and Riisgård, 1994). By modelling this interaction more carefully the volume pathways and network connectivity can visualize this mechanism in high detail.

Chapter 5

Conclusion

In this thesis, Lagrangian trajectories in the flow around a reef canopy are analysed, revealing pathways of entrainment into the canopy and showing the structure of connectivity in the local ecosystem.

Lagrangian trajectories are a powerful tool to visualise the transport of water that sedentary organisms depend on. Eddies in wakes of larger organisms entrain water from higher in the water column down towards more secluded organisms. In regions where anthropogenic activity has led to a reduction in coral cover, the entrainment of water from higher in the water column may increase. The total volume flux is the amount of incoming water that passes each organism. This roughly quantifies the time it takes for water around an organism to be refreshed. This could give an indication for which organisms are susceptible to hypoxic conditions because the depleting oxygen levels are not replenished by fresh water.

To generate accurate and continuous trajectories in the layer near the solid-fluid boundary, three particle boundary conditions at the solid-fluid interface have been defined. Based on the idea that the velocity becomes entirely tangential in the limit towards the boundary, a parabolic profile for the normal component of the velocity was implemented. That successfully reduced the amount of particles that get stuck on the solid objects to zero.

In general, the effects of waves and the spacing between organisms have a similar effect on the influx of water from the boundary and the network connectivity. They interact and reinforce each other by enabling larger eddies to form, which increases both entrainment into the reef canopy and the distance that particles travel before they interact with another organism. Below, the effects of organism spacing and waves will be summarized separately.

In the simulations with removed organisms the water entering the interaction layers comes from higher up in the water column, even though some of the tallest organisms had been removed. Under wave conditions the volume flux towards the first organisms increases or stays the same for all remaining objects. Without waves the effect is very mixed. For the total volume flux, all particles regardless of whether they have already been in an interaction layer, organism spacing increases the flux to almost all objects when waves are included, while it decreases the flux to almost all

objects when waves are not present. The effect of organism spacing on the network connectivity is to increase the edges between the remaining organisms, leading to a net increase in connectivity for many organisms even though some organisms that formed edges with the others were removed.

Waves decrease the height of the water column that flows into the reef canopy and interacts with the organisms. They increase the volume flux towards most organisms. The effect on the network is to decrease the edge strength of organisms of similar height in the upstream part of the domain by increasing the vertical displacement while increasing the edge strength of organisms in the part of the domain with more variation in height by entraining more particles into the canopy by eddies. This effectively increases the distance particles travel before they interact with another organism.

Sedentary organisms are at the mercy of advection of nutrients, oxygen, larvae and diseases. Because the Lagrangian transport was not specifically modelled to represent one of these particles or solutes, an increased transport can have both positive and negative consequences for the health of the organisms. It might signify an increased oxygen supply or an increased risk of disease spreading.

Bibliography

Aati, S. and Nejim, S. (2020). Identification of aircraft aerodynamic derivatives based on photogrammetry and computational fluid dynamics. *Journal of Physics: Conference Series*, 1432:12035.

Altieri, A. H. and Gedan, K. B. (2015). Climate change and dead zones. *Global Change Biology*, 21(4):1395–1406.

Andersson, A. J., Yeakel, K. L., Bates, N. R., and de Putron, S. J. (2014). Partial offsets in ocean acidification from changing coral reef biogeochemistry. *Nature Climate Change*, 4(1):56–61.

Anthony, K. R. N., Kline, D. I., Diaz-Pulido, G., Dove, S., and Hoegh-Guldberg, O. (2008). Ocean acidification causes bleaching and productivity loss in coral reef builders. *Proceedings of the National Academy of Sciences*, 105(45):17442–17446.

Arakawa, A. and Lamb, V. R. (1977). Computational Design of the Basic Dynamical Processes of the UCLA General Circulation Model. In CHANG, J. B. T. M. i. C. P. A. i. R. and Applications, editors, *General Circulation Models of the Atmosphere*, volume 17, pages 173–265. Elsevier.

Asher, S. and Shavit, U. (2019). The Effect of Water Depth and Internal Geometry on the Turbulent Flow Inside a Coral Reef. *Journal of Geophysical Research: Oceans*, 124(6):3508–3522.

Azevedo, A., Oliveira, A., Fortunato, A. B., and Bertin, X. (2009). Application of an Eulerian-Lagrangian oil spill modeling system to the Prestige accident: trajectory analysis. *Journal of Coastal Research*, pages 777–781.

Blakeway, D. (2018). Hypoxia shapes coral reefs. *PeerJ Preprints*.

Burns, J., Delparte, D., Gates, R., and Takabayashi, M. (2015). Integrating structure-from-motion photogrammetry with geospatial software as a novel technique for quantifying 3D ecological characteristics of coral reefs. *PeerJ*, 3:e1077.

Candy, A. S. (2020). Caribbean Watch.

Chen, Y., DiBiase, R. A., McCarroll, N., and Liu, X. (2019). Quantifying flow resistance in mountain streams using computational fluid dynamics modeling over structure-from-motion photogrammetry-derived microtopography. *Earth Surface Processes and Landforms*, 44(10):1973–1987.

de Bakker, D. M., van Duyl, F. C., Bak, R. P., Nugues, M. M., Nieuwland, G., and Meesters, E. H. (2017). 40 Years of benthic community change on the Caribbean reefs of Curaçao and Bonaire: the rise of slimy cyanobacterial mats. *Coral Reefs*, 36(2):355–367.

de Goeij, J. M., van Oevelen, D., Vermeij, M. J. A., Osinga, R., Middelburg, J. J., de Goeij, A. F. P. M., and Admiraal, W. (2013). Surviving in a Marine Desert: The Sponge Loop Retains Resources Within Coral Reefs. *Science*, 342(6154):108 LP – 110.

Delandmeter, P. and van Sebille, E. (2019). The Parcels v2.0 Lagrangian framework: new field interpolation schemes. *Geoscientific Model Development Discussions*, pages 1–24.

Della Penna, A., Koubbi, P., Cotté, C., Bon, C., Bost, C.-A., and d'Ovidio, F. (2017). Lagrangian analysis of multi-satellite data in support of open ocean Marine Protected Area design. *Deep Sea Research Part II: Topical Studies in Oceanography*, 140:212–221.

Delpeche–Ellmann, N. C. and Soomere, T. (2013). Using Lagrangian models to assist in maritime management of Coastal and Marine Protected Areas. *Journal of Coastal Research*, 65(65 (10065)):36–41.

Duvall, M. S., Rosman, J. H., and Hench, J. L. (2020). Estimating Geometric Properties of Coral Reef Topography Using Obstacle- and Surface-Based Approaches. *Journal of Geophysical Research: Oceans*, 125(6).

Edwards, K., Hare, J., Werner, F., and Blanton, B. (2006). Lagrangian circulation on the Southeast US Continental Shelf: Implications for larval dispersal and retention. *Continental Shelf Research*, 26(12-13):1375–1394.

Gyory, J., Mariano, A. J., and Ryan, E. H. (2013). The Caribbean Current.

Haas, A. F., Jantzen, C., Naumann, M. S., Iglesias-Prieto, R., and Wild, C. (2010). Organic matter release by the dominant primary producers in a Caribbean reef lagoon: Implication for in situ O2 availability. *Marine Ecology Progress Series*, 409(Lesser 2004):27–39.

Haller, G. (2015). Lagrangian Coherent Structures. *Annual Review of Fluid Mechanics*, 47(1):137–162.

Harris, D. L., Rovere, A., Casella, E., Power, H., Canavesio, R., Collin, A., Pomeroy, A., Webster, J. M., and Parravicini, V. (2018). Coral reef structural complexity provides important coastal protection from waves under rising sea levels. *Science Advances*, 4(2):eaao4350.

Hoegh-Guldberg, O., Mumby, P. J., Hooten, A. J., Steneck, R. S., Greenfield, P., Gomez, E., Harvell, C. D., Sale, P. F., Edwards, A. J., Caldeira, K., Knowlton, N., Eakin, C. M., Iglesias-Prieto, R., Muthiga, N., Bradbury, R. H., Dubi, A., and Hatziolos, M. E. (2007). Coral Reefs Under Rapid Climate Change and Ocean Acidification. *Science*, 315(5820):1811–1811.

Hughes, T. P. (1994). Catastrophes, Phase Shifts, and Large-Scale Degradation of a Caribbean Coral Reef. *Science*, 265(5178):1547–1551.

Hughes, T. P., Baird, A. H., Bellwood, D. R., Card, M., Connolly, S. R., Folke, C., Grosberg, R., Hoegh-Guldberg, O., Jackson, J. B. C., Kleypas, J., Lough, J. M., Marshall, P., Nyström, M., Palumbi, S. R., Pandolfi, J. M., Rosen, B., and Roughgarden, J. (2003). Climate change, human impacts, and the resilience of coral reefs. *Science (New York, N.Y.)*, 301(5635):929–933.

Jackson, J., Donovan, M., Cramer, K., and Lam, V. (2014). *Status and Trends of Caribbean Coral Reefs: 1970-2012*.

Lange, M. and van Sebille, E. (2017). Parcels v0.9: prototyping a Lagrangian Ocean Analysis framework for the petascale age.

Larsen, P. S. and Riisgård, H. U. (1994). The Sponge Pump. *Journal of Theoretical Biology*, 168(1):53–63.

LASKER, H. R. (1979). LIGHT DEPENDENT ACTIVITY PATTERNS AMONG REEF CORALS: MONTASTREA CAVERNOSA. *The Biological Bulletin*, 156(2):196–211.

Leggat, W. P., Camp, E. F., Suggett, D. J., Heron, S. F., Fordyce, A. J., Gardner, S., Deakin, L., Turner, M., Beeching, L. J., Kuzhiumparambil, U., Eakin, C. M., and Ainsworth, T. D. (2019). Rapid Coral Decay Is Associated with Marine Heatwave Mortality Events on Reefs. *Current biology : CB*, 29(16):2723–2730.

Leon, J., Roelfsema, C. M., Saunders, M. I., and Phinn, S. R. (2015). Measuring coral reef terrain roughness using 'Structure-from-Motion' close-range photogrammetry. *Geomorphology*, 242:21–28.

Levy, O., Dubinsky, Z., Achituv, Y., and Erez, J. (2006). Diurnal polyp expansion behavior in stony corals may enhance carbon availability for symbionts photosynthesis. *Journal of Experimental Marine Biology and Ecology*, 333(1):1–11.

Lowe, R., Shavit, U., Falter, J., Koseff, J., and Monismith, S. (2008). Modeling flow in coral communities with and without waves: A synthesis of porous media and canopy flow approaches. *Limnology and Oceanography*, 53:2668–2680.

Lowe, R. J., Falter, J. L., Bandet, M. D., Pawlak, G., Atkinson, M. J., Monismith, S. G., and Koseff, J. R. (2005a). Spectral wave dissipation over a barrier reef. *Journal of Geophysical Research*, 110(C4):C04001.

Lowe, R. J., Koseff, J. R., and Monismith, S. G. (2005b). Oscillatory flow through submerged canopies: 1. Velocity structure. *Journal of Geophysical Research C: Oceans*, 110(10):1–17.

Lynch, D. R., Greenberg, D. A., Bilgili, A., McGillicuddy, D. J., Manning, J. P., and Aretxabaleta, A. L. (2014). *Particles in the coastal ocean : theory and applications*. Cambridge University Press.

Mariano, A., Kourafalou, V., Srinivasan, A., Kang, H., Halliwell, G., Ryan, E., and Roffer, M. (2011). On the modeling of the 2010 Gulf of Mexico Oil Spill. *Dynamics of Atmospheres and Oceans*, 52(1-2):322–340.

Maximenko, N., Corradi, P., Law, K. L., Van Sebille, E., Garaba, S. P., Lampitt, R. S., Galgani, F., Martinez-Vicente, V., Goddijn-Murphy, L., Veiga, J. M., Thompson, R. C., Maes, C., Moller, D., Löscher, C. R., Addamo, A. M., Lamson, M. R., Centurioni, L. R., Posth, N. R., Lumpkin, R., Vinci, M., Martins, A. M., Pieper, C. D., Isobe, A., Hanke, G., Edwards, M., Chubarenko, I. P., Rodriguez, E., Aliani, S., Arias, M., Asner, G. P., Brosich, A., Carlton, J. T., Chao, Y., Cook, A.-M., Cundy, A. B., Galloway, T. S., Giorgetti, A., Goni, G. J., Guichoux, Y., Haram, L. E., Hardesty, B. D., Holdsworth, N., Lebreton, L., Leslie, H. A., Macadam-Somer, I., Mace, T., Manuel, M., Marsh, R., Martinez, E., Mayor, D. J., Le Moigne, M., Molina Jack, M. E., Mowlem, M. C., Obbard, R. W., Pabortsava, K., Robberson, B., Rotaru, A.-E., Ruiz, G. M., Spedicato, M. T., Thiel, M., Turra, A., and Wilcox, C. (2019). Toward the Integrated Marine Debris Observing System. *Frontiers in Marine Science*, 6:447.

Monismith, S. G., Rogers, J. S., Koweek, D., and Dunbar, R. B. (2015). Frictional wave dissipation on a remarkably rough reef. *Geophysical Research Letters*, 42(10):4063–4071.

Osinga, R., Derksen-Hooijberg, M., Wijgerde, T., and Verreth, J. A. J. (2017). Interactive effects of oxygen, carbon dioxide and flow on photosynthesis and respiration in the scleractinian coral Galaxea fascicularis. *The Journal of experimental biology*, 220(Pt 12):2236–2242.

Özgökmen, T. M., Fischer, P. F., Duan, J., and Iliescu, T. (2004). Entrainment in bottom gravity currents over complex topography from three-dimensional nonhydrostatic simulations. *Geophysical Research Letters*, 31(13):1–4.

Parra Peñuela, H. G., Angulo Morales, V., and Gaona-García, E. (2019). Multiphase CFD Simulation of Photogrammetry 3D Model for UAV Crop Spraying. pages 812–822.

Péquignet, A.-C., Becker, J. M., Merrifield, M. A., and Boc, S. J. (2011). The dissipation of wind wave energy across a fringing reef at Ipan, Guam. *Coral Reefs*, 30(S1):71–82.

Pujol, D., Abdolahpour, M., Lavery, P. S., McMahon, K., and Oldham, C. (2019). Flow velocity and nutrient uptake in marine canopies. *Marine Ecology Progress Series*, 622(July):17–30.

Rogers, C. and Miller, J. (2006). Permanent 'phase shifts' or reversible declines in coral cover? Lack of recovery of two coral reefs inSt. John, US Virgin Islands. *Marine Ecology Progress Series*, 306:103–114.

Silveira, C. B., Roach, T. N. F., Villela, H., Barno, A., Reyes, B., Rubio-Portillo, E., Le, T., Mead, S., Hatay, M., Luque, A., Wegley-Kelly, L., Vermeij, M., Bailey, B., Takeshita, Y., Haas, A., and Rohwer, F. (2018). Biophysical and physiological causes of coral reef microbialization. *bioRxiv*, page 495481.

Suara, K., Khanarmuei, M., Ghosh, A., Yu, Y., Zhang, H., Soomere, T., and Brown, R. J. (2020). Material and debris transport patterns in Moreton Bay, Australia: The influence of Lagrangian coherent structures. *Science of The Total Environment*, 721:137715.

Sweatman, H., Delean, S., and Syms, C. (2011). Assessing loss of coral cover on Australia's Great Barrier Reef over two decades, with implications for longer-term trends. *Coral Reefs*, 30(2):521–531.

van Rooijen, A., Lowe, R., Rijnsdorp, D. P., Ghisalberti, M., Jacobsen, N. G., and McCall, R. (2020). Wave-Driven Mean Flow Dynamics in Submerged Canopies. *Journal of Geophysical Research: Oceans*, 125(3):1–21.

van Sebille, E., Aliani, S., Law, K. L., Maximenko, N., Alsina, J. M., Bagaev, A., Bergmann, M., Chapron, B., Chubarenko, I., Cózar, A., Delandmeter, P., Egger, M., Fox-Kemper, B., Garaba, S. P., Goddijn-Murphy, L., Hardesty, B. D., Hoffman, M. J., Isobe, A., Jongedijk, C. E., Kaandorp, M. L. A., Khatmullina, L., Koelmans, A. A., Kukulka, T., Laufkötter, C., Lebreton, L., Lobelle, D., Maes, C., Martinez-Vicente, V., Morales Maqueda, M. A., Poulain-Zarcos, M., Rodríguez, E., Ryan, P. G., Shanks, A. L., Shim, W. J., Suaria, G., Thiel, M., van den Bremer, T. S., and Wichmann, D. (2020). The physical oceanography of the transport of floating marine debris. *Environmental Research Letters*, 15(2):023003.

Vic, C., Gula, J., Roullet, G., and Pradillon, F. (2018). Dispersion of deep-sea hydrothermal vent effluents and larvae by submesoscale and tidal currents. *Deep-Sea Research Part I: Oceanographic Research Papers*, 133(March 2017):1–18.

Yu, X., Rosman, J. H., and Hench, J. L. (2018). Interaction of Waves with Idealized High-Relief Bottom Roughness. *Journal of Geophysical Research: Oceans*, 123(4):3038–3059.

Appendix A

Sensitivity

A.1 Boundary Conditions

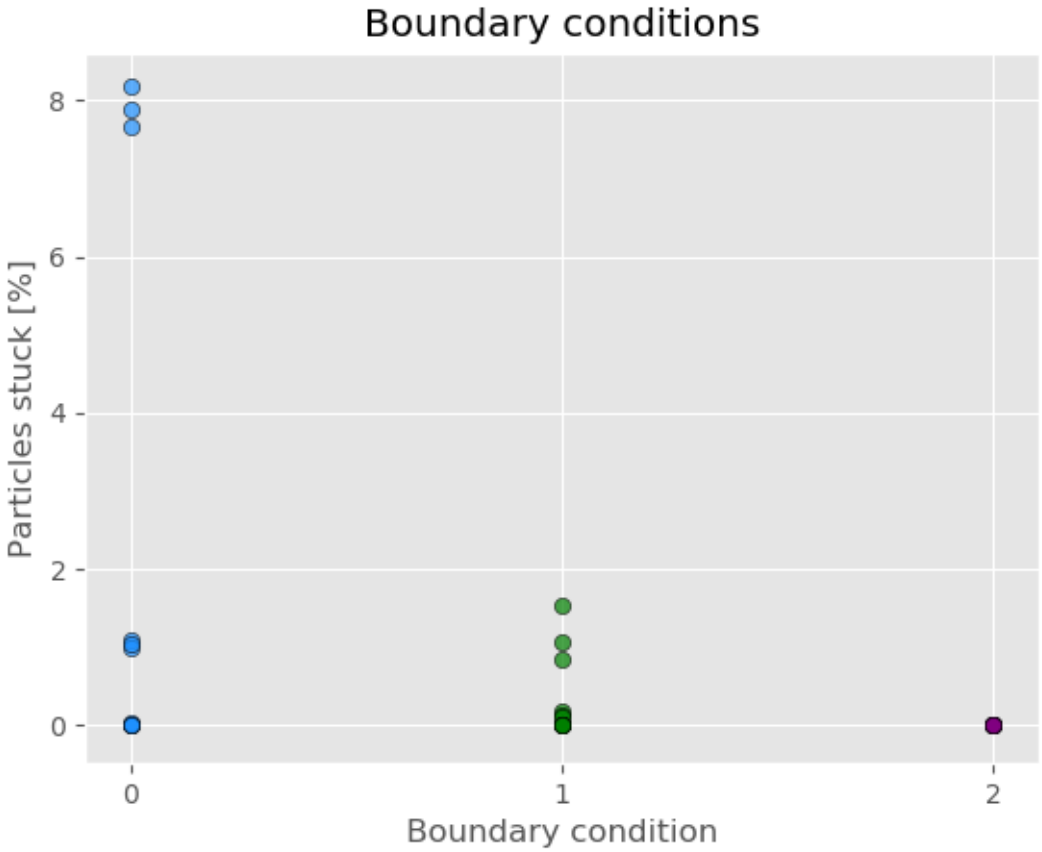

Figure A.1: Percentage of particles stuck on objects depending on the boundary conditions used. Boundary condition 0 represents the incorrect interpolation that follows from Parcels scheme not being compatible with the output at the center of gridcells. Boundary condition 1 represents the correct linear interpolation that does not parametrise the subgrid anisotropy. Boundary condition 2 is the boundary condition applied in this thesis.

A.2 Object area

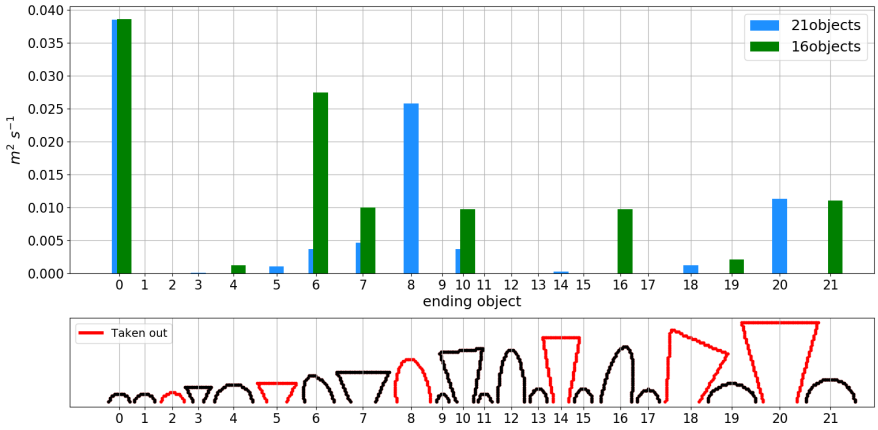

(a) Flow: Parabolic + Waves Boundary Condition: parabolic-linear Boundary Layer Thickness: 5 cm

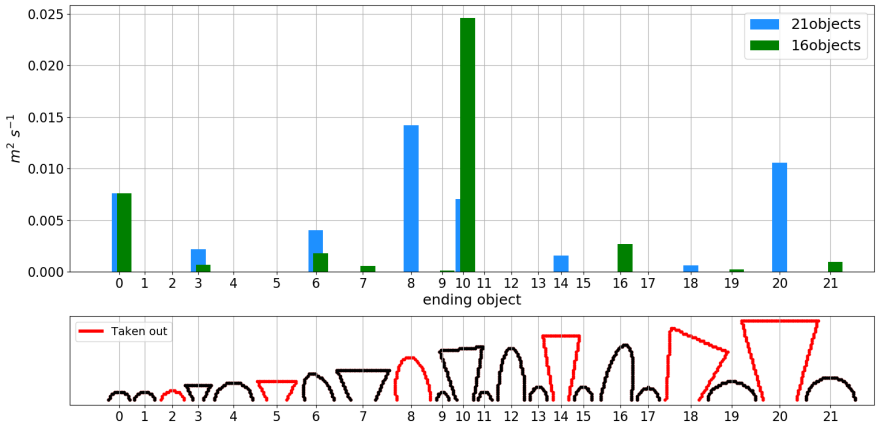

(b) Flow: Parabolic Boundary Condition: parabolic-linear Boundary Layer Thickness: 5 cm

Figure A.2: The 2D volume flux of water to the first object it enters the boundary layer of. This is the volume flux not as a function of the surface length of the receiving object. This is a better representation of the distribution of the incoming particles, but a worse representation of the object conditions